

Supplementary Information

A Bioinspired In-Materia Analogue Photoelectronic Reservoir Computing for Human Action Processing

*Hangyuan Cui¹, Yu Xiao³, Yang Yang¹, Mengjiao Pei¹, Shuo Ke¹, Xiao Fang¹,
Lesheng Qiao¹, Kailu Shi¹, Haotian Long¹, Weigao Xu⁴, Pingqiang Cai⁵, Peng Lin^{3*},
Yi Shi^{1*}, Qing Wan^{2*}, Changjin Wan^{1,2*}*

¹School of Electronic Science and Engineering, National Laboratory of Solid-State Microstructures, Nanjing University, Nanjing 210023, P. R. China.

²Yongjiang Laboratory (Y-LAB), Ningbo 315202, China.

³College of Computer Science and Technology, ~~Zhejiang University, Hangzhou, China,~~ State Key Laboratory of Brain Machine Intelligence, Zhejiang University, Hangzhou 310058, China.

⁴Key Laboratory of Mesoscopic Chemistry, School of Chemistry and Chemical Engineering, Nanjing University, Nanjing 210023, China

⁵Jiangsu Key Laboratory of Molecular Medicine, Medical School, Nanjing University, Nanjing 210023, P. R. China.

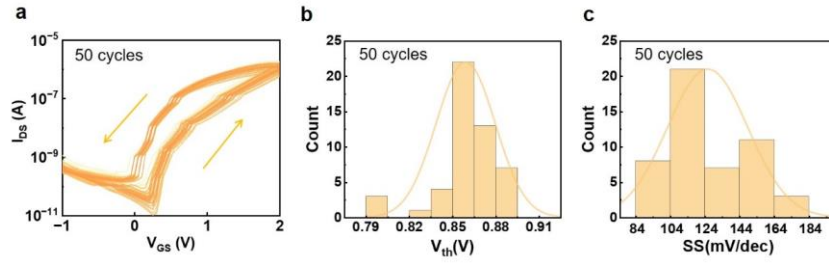
*Correspondence and requests for materials should be addressed to Changjin Wan (cjwan@nju.edu.cn), Qing Wan (wanqing@nju.edu.cn), Yi Shi (yshi@nju.edu.cn) and Peng Lin (penglin@zju.edu.cn).

This PDF file includes:

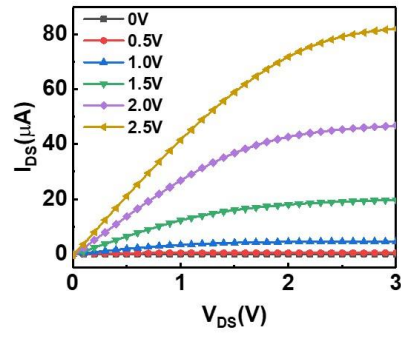
Supplementary Figures 1 to 30 (Pages S3-S32)

Supplementary Tables 1 to 3 (Page S33-S35)

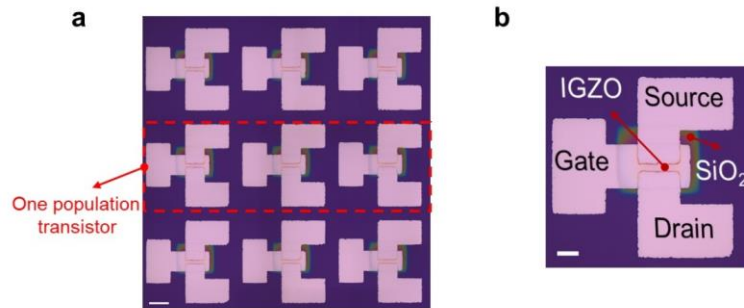
Supplementary Notes 1 to 5 (Page S36-S39)



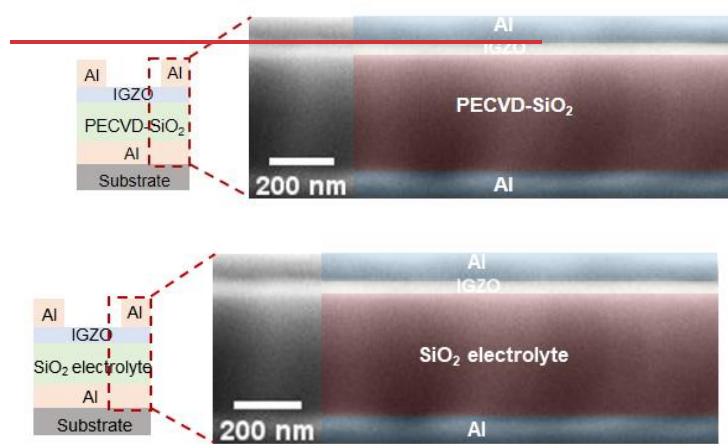
Supplementary Figure 1 | Transfer characteristics of IGZO transistor. a, Device's transfer curves under 50 testing cycles. **b,** The statistical histogram of threshold voltages (V_{th}) under 50 testing cycles. **c,** The statistical histogram of subthreshold swing (SS) under 50 testing cycles.



Supplementary Figure 2 | Output characteristic of IGZO transistor. Output curves with V_{GS} from 0 V to 2.5 V with a voltage step of 0.5 V.

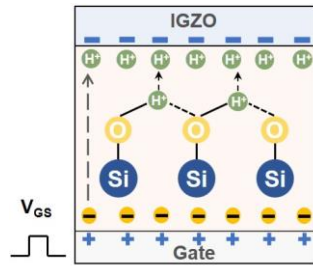


Supplementary Figure 3 | Close-up images of partial IGZO transistor array and one device. a, The micrograph close-up image of partial device array (scale bar: 400 μm). **b,** The micrograph close-up image of one device (scale bar: 200 μm).

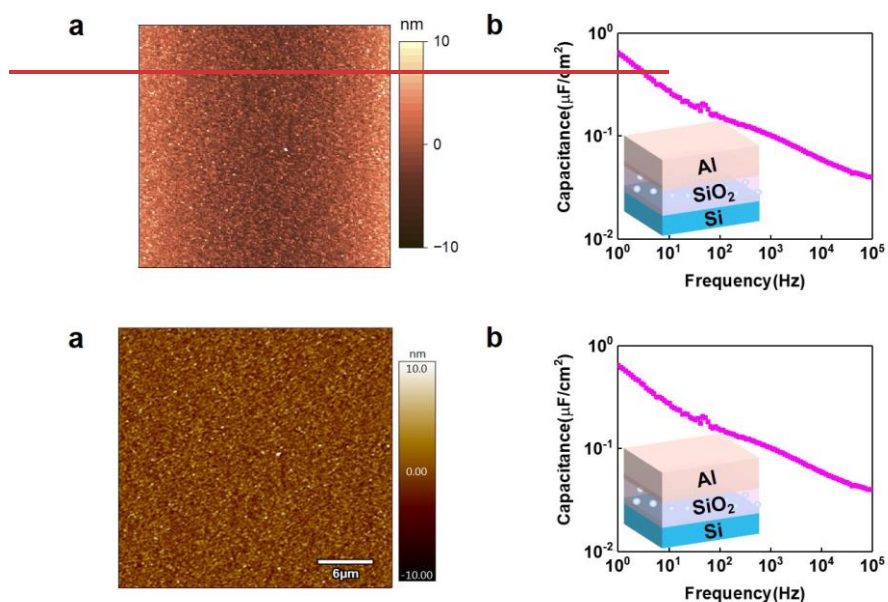


带格式的: 缩进: 首行缩进: 2.5 字符

Supplementary Figure 4 | The cross-sectional SEM image of IGZO transistor.

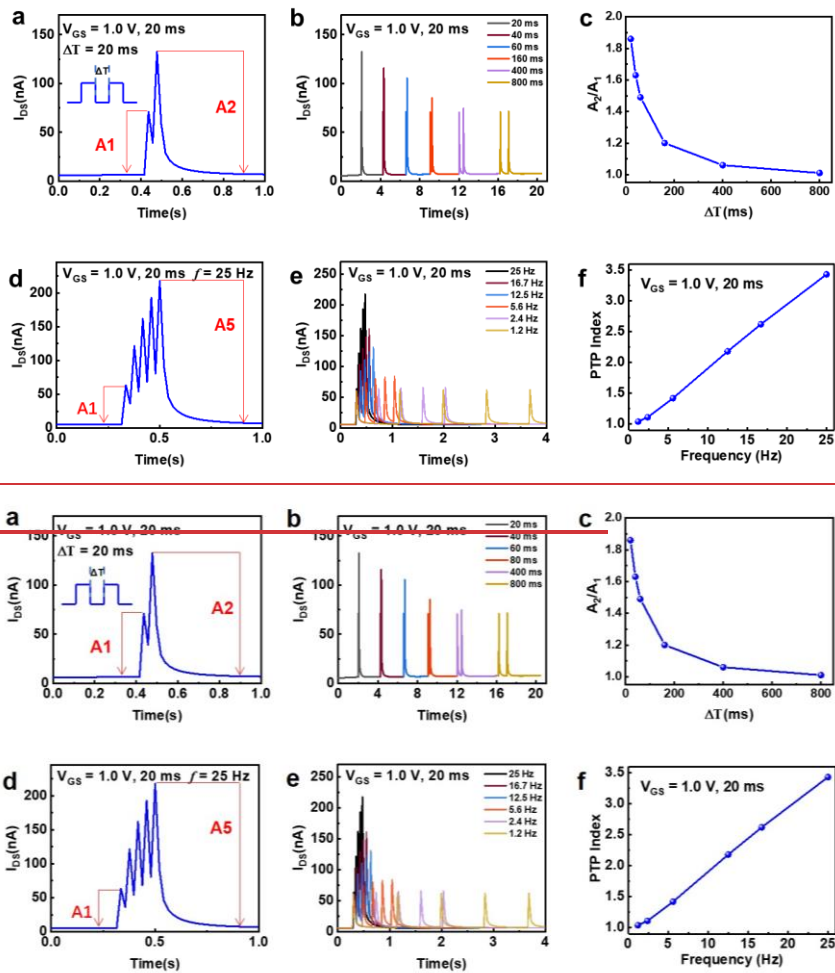


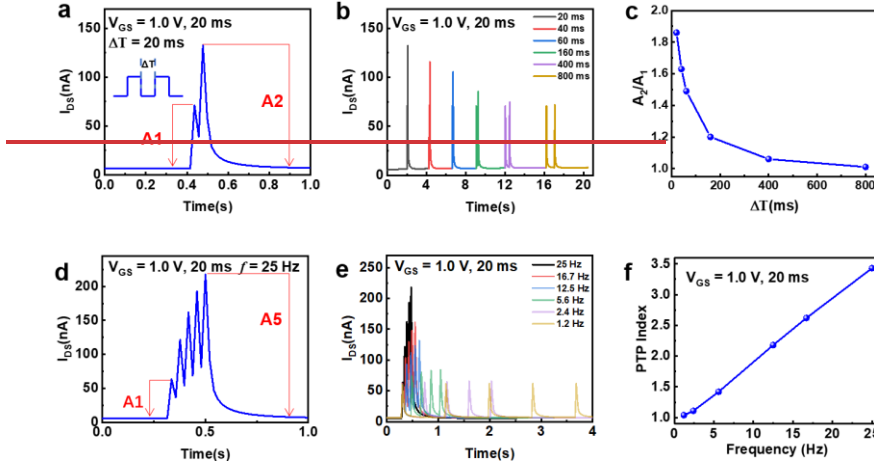
Supplementary Figure 5 | The physical mechanism diagram of EDL coupling effects. EDL coupling effect refers to the electrostatic coupling between electrons in IGZO and ions in SiO₂ electrolyte which is deposited by PECVD under low temperature condition and possess a loose and porous structure. H⁺ protons in such an electrolyte can be drifted along silicon–oxygen bonds under an electrical field. By applying positive gate voltages, H⁺ protons would be accumulated at the channel/electrolyte interface, which induce the image carriers through IGZO channel and forms the electrical-double-layer.



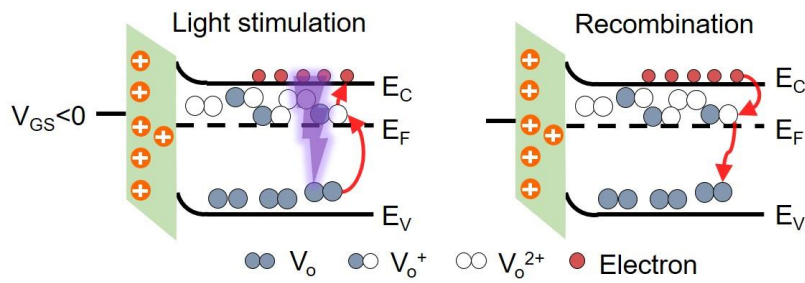
Supplementary Figure 6 | Characterization and capacitance characteristic of PECVD-SiO₂ film. **a**, AFM image of PECVD-SiO₂ film shows a RMS of 1.733 nm. **b**, Capacitance-frequency characteristic of PECVD-SiO₂ film tested on a Al-SiO₂-Si sandwich structure, indicating a ~0.6 μF/cm².

|

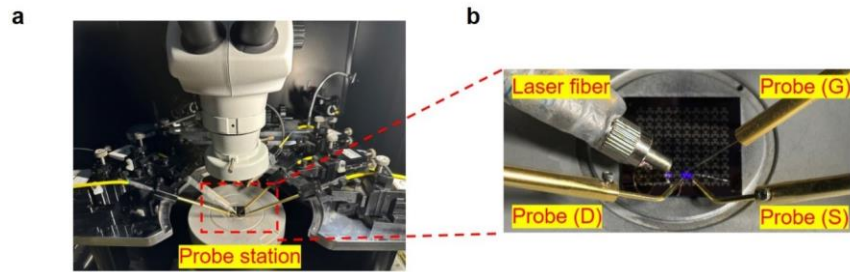




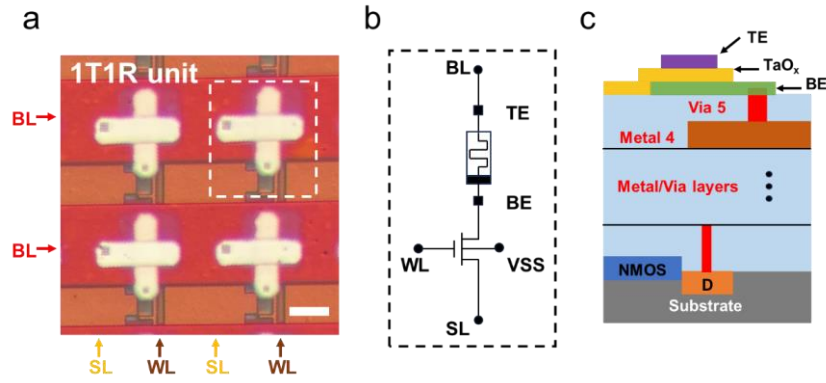
Supplementary Figure 7 | Electrical synaptic plasticity emulations of IGZO transistor. **a**, Typical PPF characteristic with a time interval of 20 ms. **b**, PPF performances with different time intervals (20, 40, 60, 160, 400, 800 ms, respectively). **c**, Changes of facilitation ratio (A_2/A_1) with time interval. **d**, Typical PTP property triggered by five consecutive pulses with frequency of 25 Hz. **e**, PTP performances at different frequencies (1.2, 2.4, 5.6, 12.5, 16.7, 25 Hz, respectively). **f**, PTP index (A_5/A_1) changes with pulse frequencies.



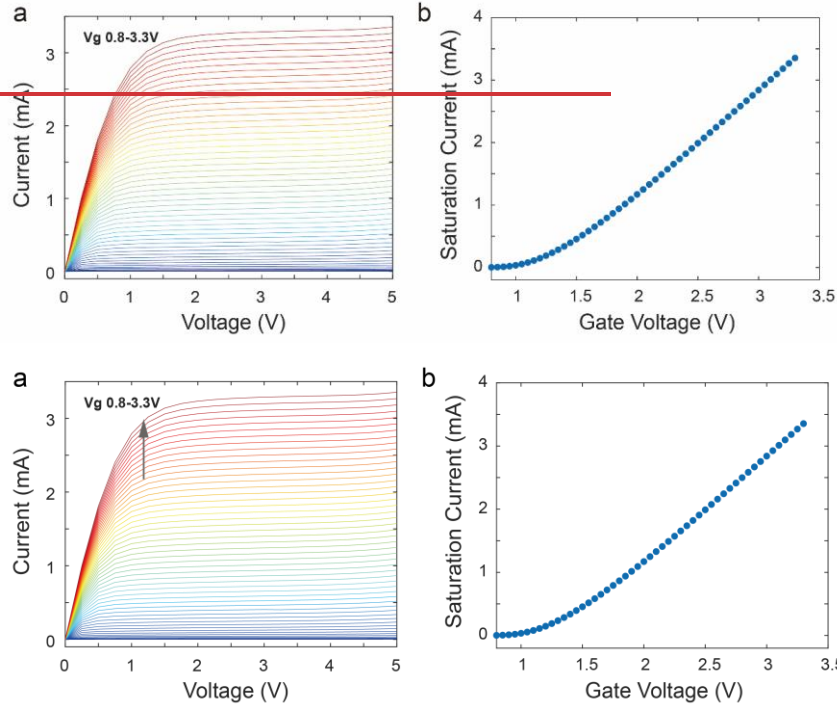
Supplementary Figure 8 | Schematic diagram of the combined effect of PPC and EDL coupling of IGZO transistor. Negative bias would lead to the upward bending of the band, due to the EDL effect. Under a light illumination, a negative gate voltage would decrease the channel conductance, leading to a decreased decay time. The decrement is dependent on the absolute value of the negative gate voltage.



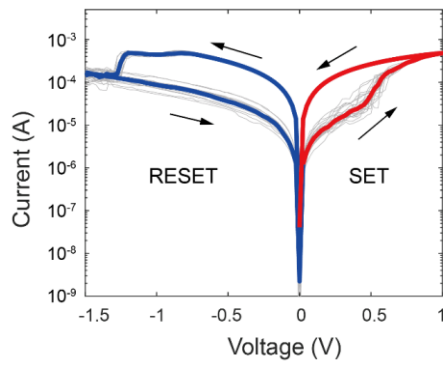
Supplementary Figure 9 | Hardware operation system used for IGZO transistor array. **a**, Optical image of the measurement system (in a probe station) and the lighting system (a fiber coupled laser module, CNI Laser PGL-FC-405 nm). **b**, Optical image of photoelectronic transistor measured with probes and laser fiber.



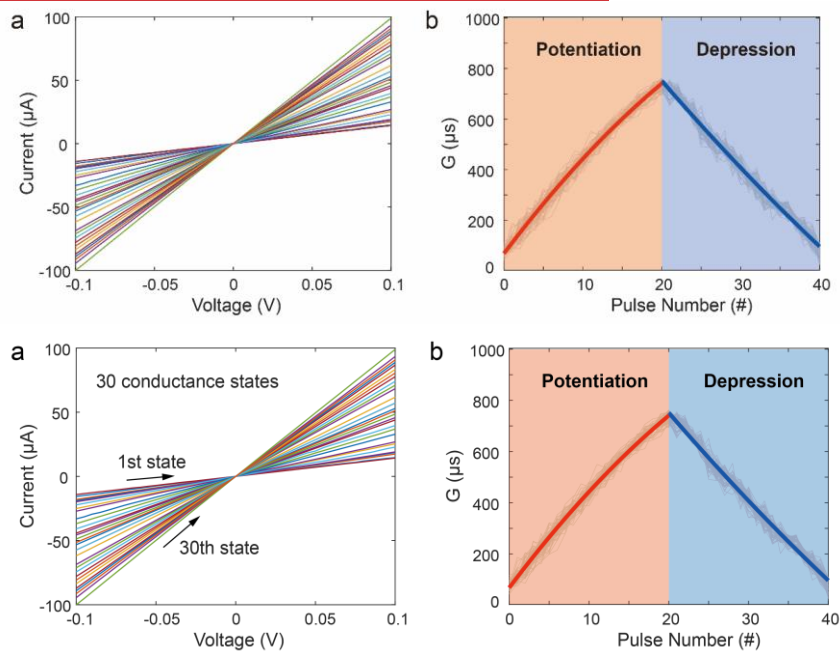
Supplementary Figure 10 | Detailed design structure of 1T1R unit. a, Optical image of 1T1R unit in an array using commercial 180 nm design rules (scale bar: 10 μm). **b,** The detail circuit schematic of 1T1R unit structure. **c,** The cross-sectional structure showing the integration of TaO_x-based memristor on top of CMOS chip.



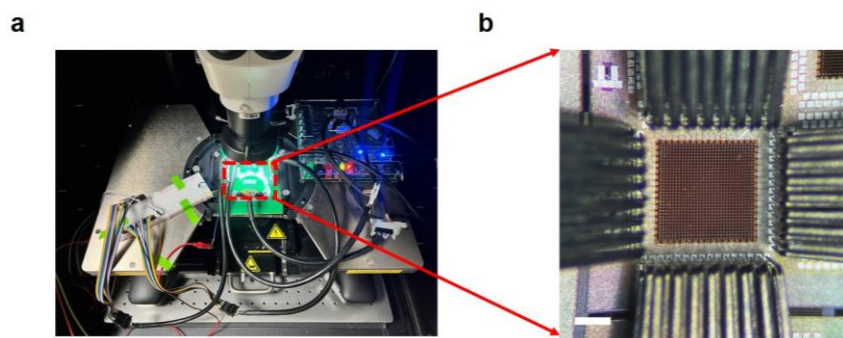
Supplementary Figure 11 | Output characteristics of the transistor (1T) in the 1T1R structure. **a,** The output characteristics of the transistor in a 1T1R device under different gate voltages (V_g) from 0.8_V to 3.3_V with a step of 0.05_V. **b,** The saturation I_{DS} current plotted as a function of V_g .



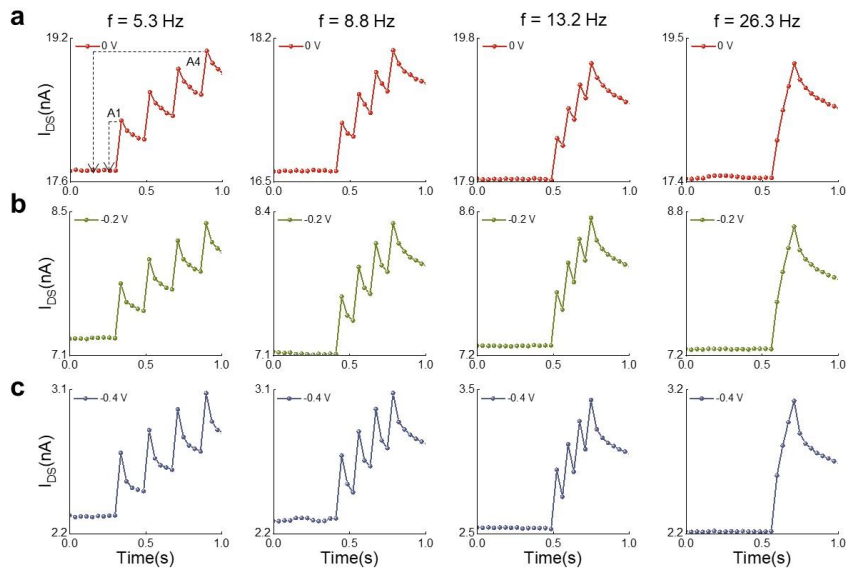
Supplementary Figure 12 | The DC sweep curves of 1T1R device. DC sweep curves over 20 testing cycles under transistor gate voltages of 1.8_V for SET and 5 V for RESET, respectively.



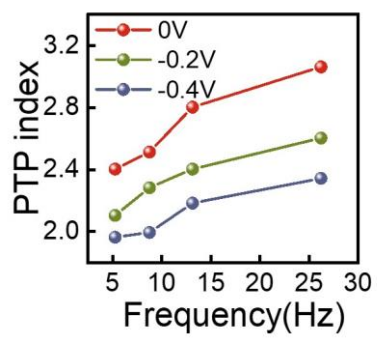
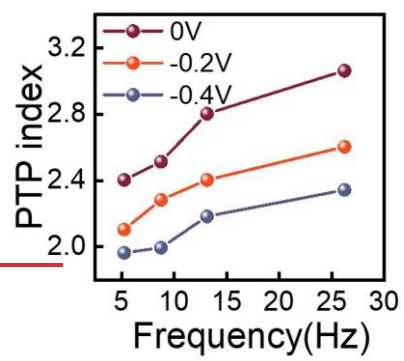
Supplementary Figure 13 | Analog synapse characteristics of 1T1R device. a, The I-V curve for 30 conductance states of one 1T1R cell from -0.1 V to 0.1 V. **b,** Conductance dynamics during 50 cycles of potentiation and depression for one 1T1R cell.



Supplementary Figure 14 | Hardware operation system used for 1T1R array. **a**, Optical image of the measurement system for 1T1R array during inference process. **b**, Optical image of 1T1R array measured with a probe card (scale bar: 300 μm).

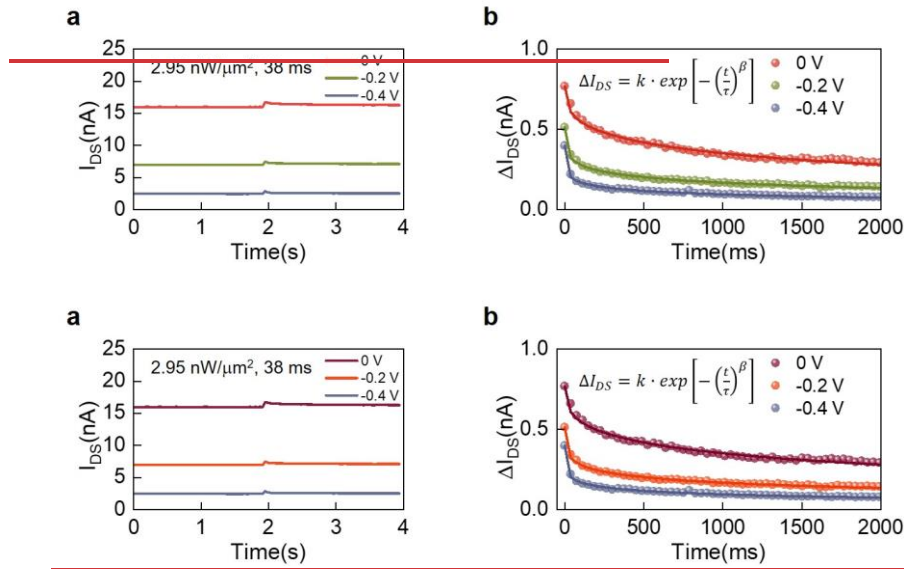


Supplementary Figure 15 | Photoelectric synergistic synaptic plasticity of IGZO phototransistor. a-c, PTP performances triggered by four consecutive light pulses of different frequencies (5.3, 8.8, 13.2, 26.3 Hz, respectively) by gate bias voltages of 0 V, -0.2 V, -0.4 V, respectively.

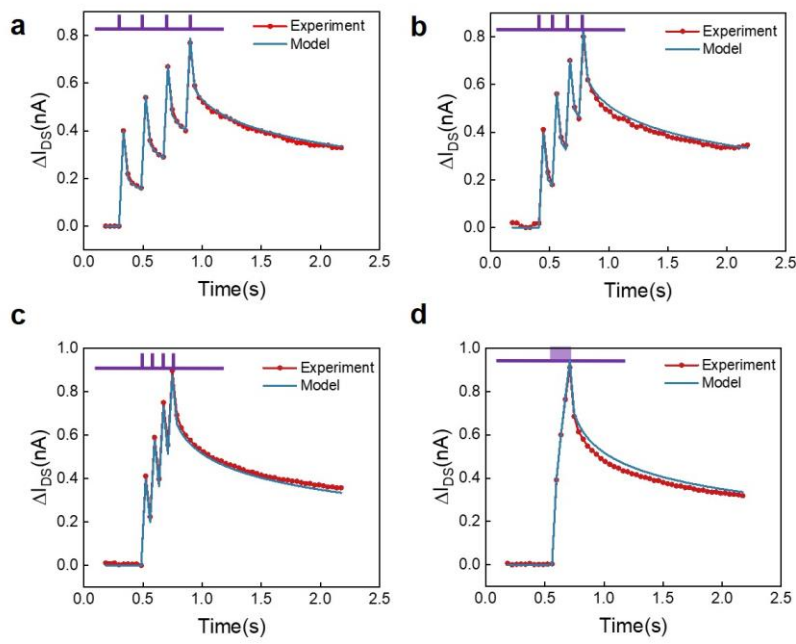


Supplementary Figure 16 | PTP index (A_4/A_1) changes with pulse frequencies by

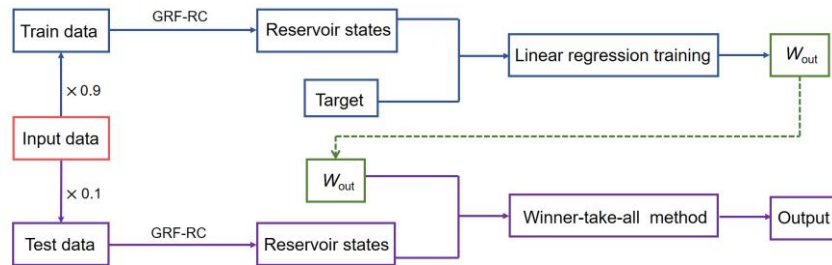
gate bias voltages of 0 V, -0.2 V, -0.4 V, respectively.



Supplementary Figure 17 | Parametric fitting of relaxation properties. **a**, PPC characteristics modulated by different gate voltages. The light stimulation in all cases are UV light with a width of 38 ms and light power of $2.95-2.95 \text{ nW} \cdot \mu\text{m}^{-2} \text{ nW}/\mu\text{m}^2$. **b**, Formula fitting for relaxation characteristics modulated by gate voltages of 0 V, -0.2 V, -0.4 V, respectively, where the symbols represent measured data and the curves are fitted from the experimental data.

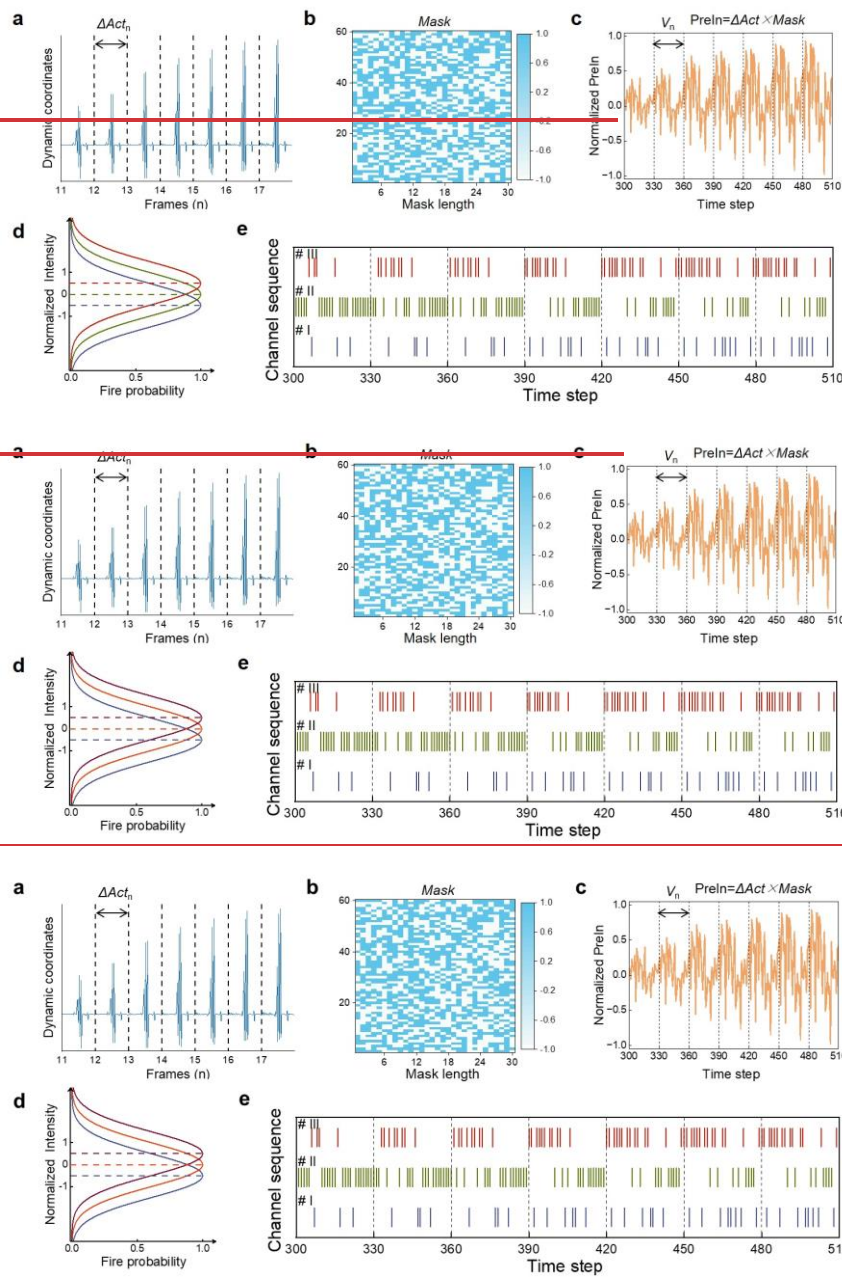


Supplementary Figure 18 | The comparison of reservoir currents obtained by device model and experiments under four light pulses with V_{GS} of -0.4 V.



Supplementary Figure 19 | The scheme of training and testing processes. Original dataset is randomly divided into training and testing set at a ratio of 9:1. The reservoir states obtained from training set are used to train the output weights (W_{out}) by one-step linear regression. The resulting weight matrixes are multiplied with the reservoir states generated by testing set and the final result is output in a winner-take-all manner.

设置了格式: 字体: 非倾斜



Supplementary Figure 20 | Specific encoding processes in the UTD-MHAD dataset standard test. **a**, Examples of ΔAct_n in the action “Draw X” of UTD-MHAD dataset. **b**, An example of mask matrix ($M=30$). **c**, An example of PreIn corresponding to ΔAct_n .

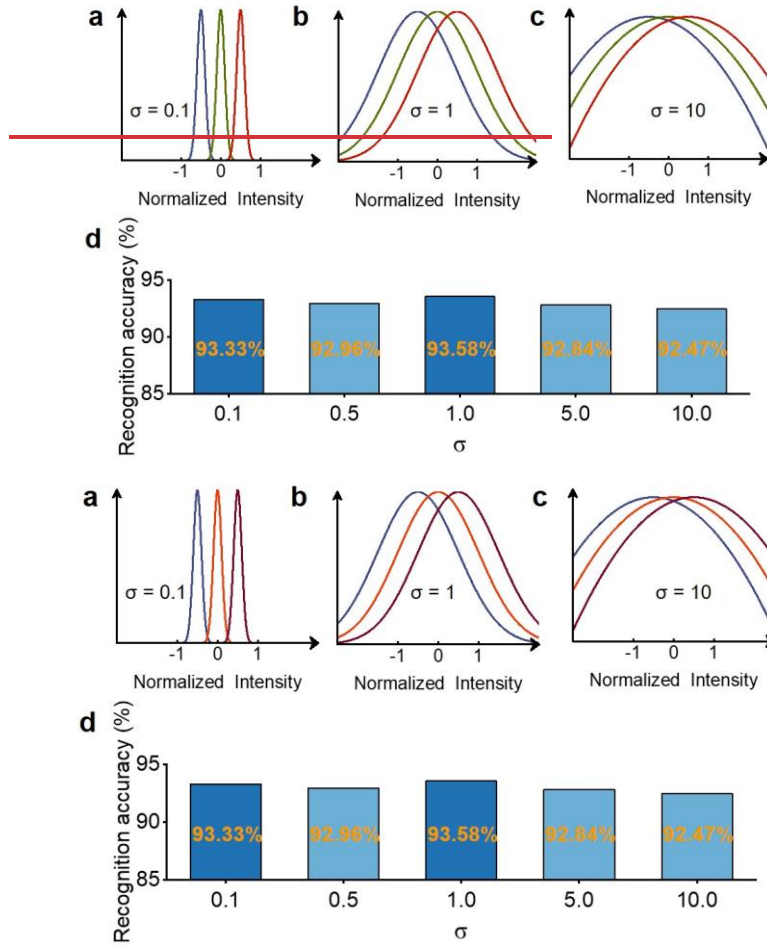
设置了格式: 字体: 非倾斜

设置了格式: 字体: 非倾斜

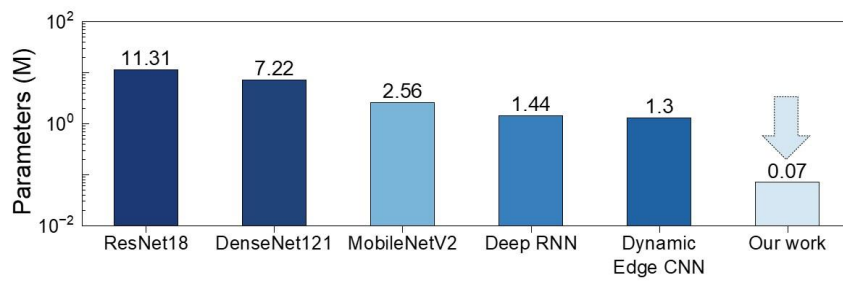
设置了格式: 字体: 非倾斜

设置了格式: 字体: 非倾斜

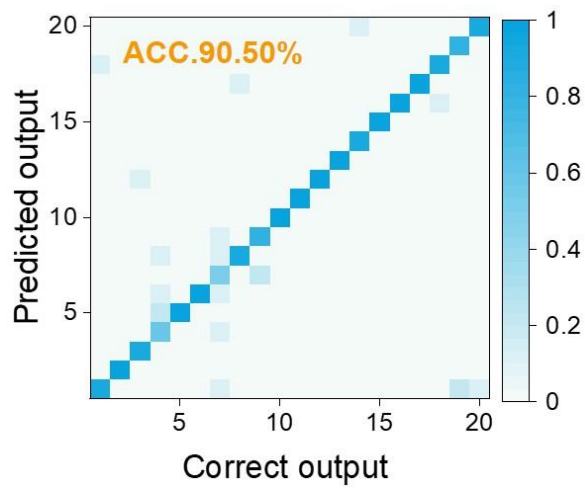
in Fig. S20a with the mask matrix in Fig. S20b. **d**, Schematic diagram of the distribution of Gaussian receptive fields. **e**, The encoded light pulse trains within partial time sections.



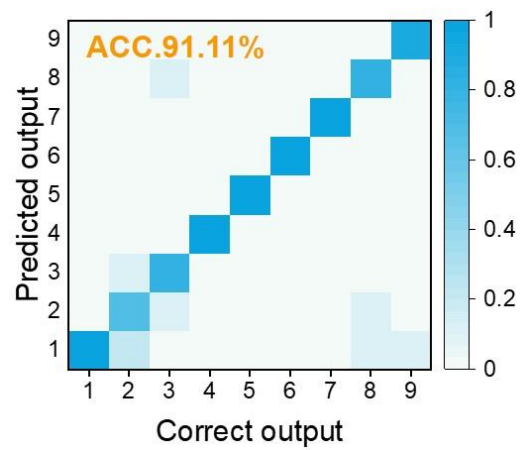
Supplementary Figure 21 | The impact of the standard deviation σ of gaussian receptive fields on the recognition results. **a-c**, Schematic diagram of the distribution of gaussian receptive fields with different deviation σ ($\sigma=0.1$, 1, and 10, respectively). **d**, Recognition results on UTD-MHAD dataset by bioinspired in-materia reservoir computing with different standard deviation, which are 93.33%, 92.96%, 93.58%, 92.84%, and 92.47%, respectively.



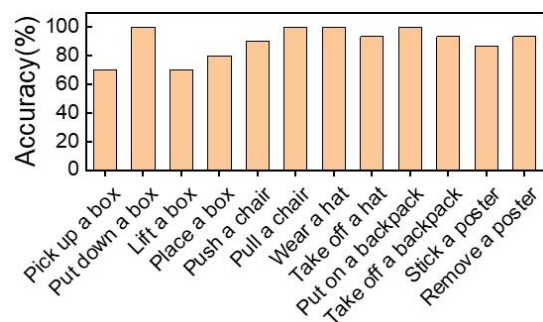
Supplementary Figure 22 | Comparison of model parameter number based on UTD-MHAD dataset testing. The comparison of model parameter number among our bioinspired in-materia reservoir computing and various machine learning algorithms based on UTD-MHAD dataset testing.



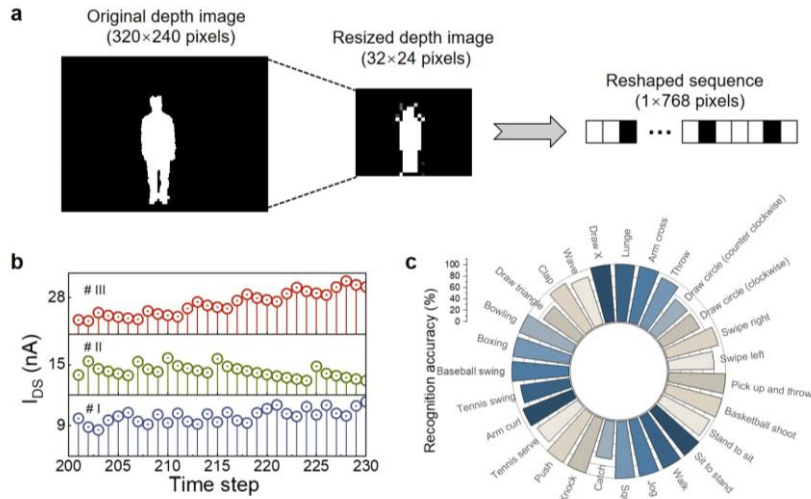
Supplementary Figure 23 | Recognition results of MSR Action3D dataset standard test. The recognition accuracy is 90.50% by 5-time random subsampling validation method.



Supplementary Figure 24 | Recognition results of Florence 3D dataset standard test. The recognition accuracy is 91.11% by 5-time random subsampling validation method.

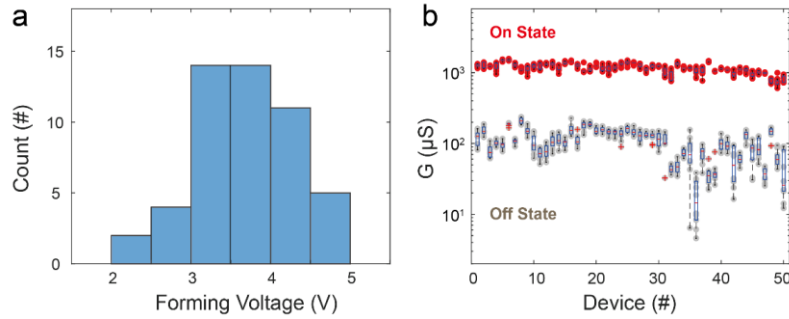


Supplementary Figure 25 | Recognition results of MSR Action Pairs dataset standard test. The recognition accuracy is 90.67% by 5-time random subsampling validation method.

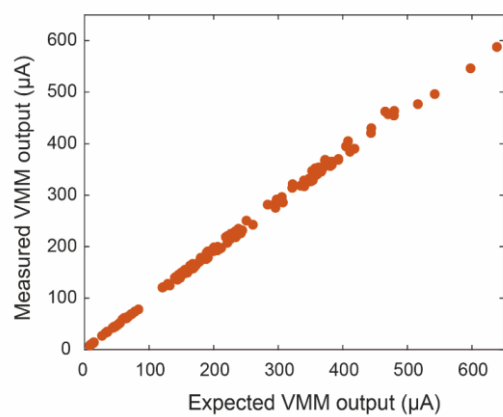


Supplementary Figure 26 | Human action recognition task based on depth images.

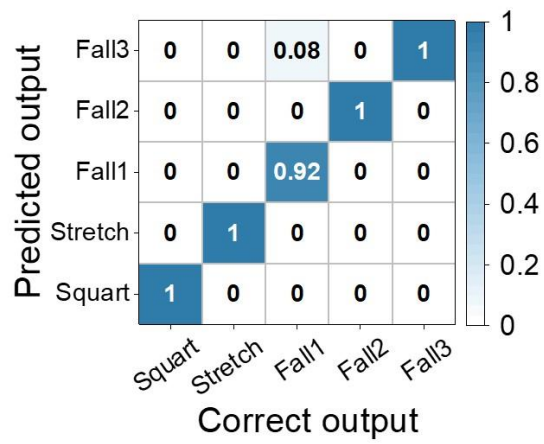
a, The preprocessing process of image resized before performing calculations. **b**, The partial example of obtained reservoir states. **c**, The recognition result with a high recognition accuracy of 92.35% on 27 action types.



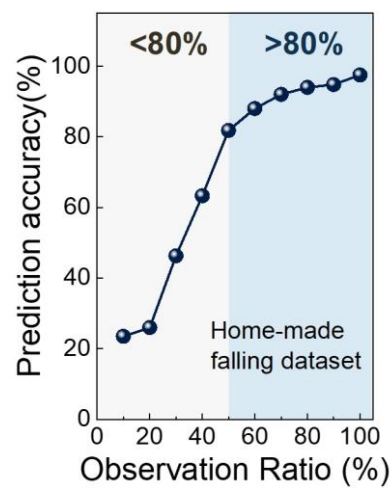
Supplementary Figure 27 | Reliable characteristics of integrated memristors in 1T1R array for the inference implementation. **a**, The forming voltages are displayed for 50 random 1T1R devices in an array. **b**, The conductance of on states and off states are measured for 50 devices over 10 cycles. The error bars represent the standard deviation of ten independent tests.



Supplementary Figure 28 | Comparison between the measured output current and the expected output current of the VMM implemented in the 1T1R array.



Supplementary Figure 29 | Recognition results of falling behaviors based on software stimulations. The recognition accuracy is 98.33%.



Supplementary Figure 30 | Prediction results of falling behaviors.

Supplementary Table 1 | Relaxation characteristic parameters in bioinspired in-material reservoir computing.

| V_{GS} (V) | κ (nA) | τ (ms) | β | I_0 (nA) |
|--------------|---------------|-------------|---------|------------|
| 0 | 0.768 | 1948 | 0.37 | 15.93 |
| -0.2 | 0.512 | 670 | 0.26 | 6.91 |
| -0.4 | 0.398 | 206 | 0.22 | 2.39 |

Supplementary Table 2 | Specific simulation parameters of bioinspired in-materialia reservoir computing on different dataset standard tests.

| Dataset | M | L | Train samples | Test samples | Cross-validation times |
|--------------------|---|-----|---------------|--------------|------------------------|
| MSR Action3D | 6 | 100 | 360 | 40 | 5 |
| Florence 3D | 4 | 30 | 162 | 18 | 5 |
| MSR ActionPairs | 8 | 60 | 270 | 30 | 5 |

Supplementary Table 3 | Comparison of different PRC devices for human action recognition.

| Reservoir layer device | Readout layer device | Application scenario | Action type number | Multiple training iterations |
|---|--|---|--------------------|------------------------------|
| Memristor ¹³ ITO/ZnO/NSTO | Software simulated ANN | Simulated motion images | 3 | Required |
| Transistor ⁵⁰ Al/IGZO/Al ₂ O ₃ /ZnO | Software simulated FCN | Inertial sensor data of action | 6 | Required |
| Memristor ⁵¹ TiN/ZnO/TiN | Software simulated fully connected layer | Standard dataset of action videos | 10 | Required |
| Memristor ⁵² Au/ZnO:N/IGZO/TiN | Software simulated MLP | Standard dataset of action videos | 10 | Required |
| Transistor Al/IGZO/SiO ₂ (This work) | Fully analog memristor array | Standard and home made dataset of action videos | 27 | Not required |

Supplementary Note 1. The physical mechanism of PPC and EDL coupling effects in EDL coupled IGZO photoelectronic transistor

IGZO is an oxide-based semiconductor with a wide band gap of ~ 3.5 eV. A UV illumination (405 nm in this work) can trigger PPC effect, which is generally considered as a result from the ionization and recombination of oxygen vacancies. Deep localized states in the IGZO channel can be ionized into shallow donor states under light illumination ($V_o \rightarrow V_o^+ + e^-$ or $V_o \rightarrow V_o^{2+} + 2e^-$). The electrons generated by this process thereby increase the channel conductance. When a light stimulation ends, accumulated electrons would recombine gradually with the triggered oxygen vacancies within a certain time. As a consequence, the channel conductance gradually decreases, exhibiting certain relaxation characteristics.

On the other hand, the EDL coupling effect refers to the electrostatic coupling between electrons in IGZO and ions in SiO_2 electrolyte as shown in Supplementary Figure 5. In our IGZO photoelectronic transistor, the SiO_2 electrolyte is used as gate dielectric, which is deposited by PECVD under low temperature condition and possess a loose and porous structure. H^+ protons in such an electrolyte can be drifted along silicon–oxygen bonds under an electrical field. By applying positive gate voltages, H^+ protons would be accumulated at the channel/electrolyte interface, which induce the carriers through IGZO channel and forms the electrical-double-layer.

The combined effect of PPC and EDL coupling is shown in Supplementary Figure 8. Negative bias would lead to the upward bending of the band, due to the EDL effect. Under a light illumination, a negative gate voltage would decrease the channel conductance, leading to a decreased decay time. The decrement is dependent on the absolute value of the negative gate voltage.

Supplementary Note 2. Modeling relaxation characteristics in bioinspired in-material reservoir computing based on PPC and EDL coupling effects

Nonlinearity and short-term memory are essential features of reservoir nodes in RC system. In bioinspired in-material reservoir computing, the inherent PPC effect of EDL coupled IGZO optoelectronic transistor provides such properties. Relaxation curves are used as activation functions. Stretched-exponential decay is used to simulate the relaxation process after light stimulation:

$$\Delta I_{DS} = \kappa \cdot \exp \left[- \left(\frac{t}{\tau} \right)^\beta \right] \quad (S1)$$

设置了格式: 字体: (默认) Times New Roman
设置了格式: 字体: Times New Roman, 非倾斜
设置了格式: 字体: Times New Roman, 非倾斜
设置了格式: 字体: Times New Roman, 非倾斜
设置了格式: 字体: Times New Roman
设置了格式: 字体: Times New Roman, 非倾斜
设置了格式: 字体: Times New Roman
设置了格式: 字体: Times New Roman, 非倾斜
设置了格式: 字体: Times New Roman
设置了格式: 字体: Times New Roman
设置了格式: 字体: Times New Roman

where parameters κ, τ, β represent current change value excited by light stimulation, relaxation time constant and stretch index, respectively. Based on such short-term memory properties, reservoir nodes are interconnected. When light pulse sequence is applied, the continuous response process of device can be fitted in an accumulation manner. For example, when a light pulse with fixed intensity and width is applied at time step t_1 in sequence (duration time (T) of time step is 38 ms in this work), the dynamic response of device at time step t_n is:

$$\Delta I_{DS} = \begin{cases} 0 & t_n < t_1 \\ \kappa \cdot \exp \left[-\left(\frac{(t_n - t_1) \cdot T}{\tau} \right)^\beta \right] & t_n \geq t_1 \end{cases} \quad (S2)$$

After this moment, when the same light pulse is applied at time step t_2 ($t_2 > t_1$) in pulse sequence, the dynamic response of device caused by this pulse is:

$$\Delta I_{DS} = \kappa \cdot \exp \left[-\left(\frac{(t_n - t_2) \cdot T}{\tau} \right)^\beta \right] \quad (t_n \geq t_2) \quad (S3)$$

The dynamic response of device caused by the two light pulses in sequence is accumulated as follows:

$$\Delta I_{DS} = \begin{cases} 0 & t_n < t_1 \\ \kappa \cdot \exp \left[-\left(\frac{(t_n - t_1) \cdot T}{\tau} \right)^\beta \right] & t_1 \leq t_n < t_2 \\ \kappa \cdot \exp \left[-\left(\frac{(t_n - t_1) \cdot T}{\tau} \right)^\beta \right] + \kappa \cdot \exp \left[-\left(\frac{(t_n - t_2) \cdot T}{\tau} \right)^\beta \right] & t_n \geq t_2 \end{cases} \quad (S4)$$

The device's response to continuous sequence comes from the accumulation of dynamic responses to light pulses at different times. The response current at each time step depends on both the stimulus at this moment and the residual relaxation current of the past moments. The output current of each time step (I_{DS}) is calculated as: $I_{DS} = \Delta I_{DS} + I_0$, where I_0 represents current of static state. Meanwhile, nonlinearity can be enriched due to proton relaxation dynamics, thereby optimizing the calculation results. Relaxation processes are different under different voltage regulations as shown in Supplementary Fig. 17, thus obtaining different relaxation parameters as shown in Supplementary Table 1.

Supplementary Note 3. Calculation process of memory capacity in bioinspired in-materialia reservoir computing

Memory capacity (MC) is a task-independent characteristic parameter in reservoir computing system, which reflects the ability of reservoir states to remember historical information. In our bioinspired in-materialia reservoir computing system, MC is calculated by reconstruction task of

binary sequences. Firstly, a binary sequence (I) consists of 0 and 1 with length of 4000 is generated randomly, which is transported to bioinspired in-materia reservoir computing system ($M=3, L=1$) to obtain the reservoir sequence (R). Then, I_{delayi} is generated by delaying I by i steps, which is used to test the reservoir's memory capacity. At each delay step i , the first 3000 points of I_{delayi} (I_{delayi} (1:3000)) and R (R (1:3000)) are regarded as target matrix Y_{target} and reservoir states matrix X respectively during training process. The output weights (W_{out}) are calculated by:

$$W_{out} = Y_{target} X^T (X X^T)^{\dagger} \quad (S5)$$

In testing process, The last 1000 points of R (R (3001:4000)) are regarded as reservoir states matrix X . The output (O_{delayi}) at each delay step i is calculated by:

$$O_{delayi} = W_{out} X \quad (S6)$$

The last 1000 points of I_{delayi} (I_{delayi} (3001:4000)) is regarded as label (Y_{delayi}). Correlation coefficient (Cor_i^2) is used to evaluate the effectiveness of reconstruction task at each delay step i by:

$$Cor_i^2 = \frac{Cov(Y_{delayi}, O_{delayi})^2}{Var(Y_{delayi}) Var(O_{delayi})} \quad (S7)$$

Where symbol Var and Cov represent variance and covariance, respectively. When the delay step i approaches from 1 to infinity, the accumulated correlation coefficients is defined as MC:

$$MC = \sum_{i=1}^{\infty} Cor_i^2 \quad (S8)$$

In our experiment, the maximum value of i is set to 3999 since the binary sequence length is 4000. In each test, thirty different sets of input (I) and mask (Mask) matrices are randomly generated, and the average of the thirty MC results is taken as the result of one test to reduce randomness. Fig. 2f shows the results of five tests with different GRF neuron number.

Supplementary Note 4. Human action recognition task based on depth images in videos by bioinspired in-materia reservoir computing.

UTD-MHAD dataset was used for benchmark test to evaluate the efficacy on human action recognition task based on depth images in videos. As a multimodal dataset, not only skeleton information of each frame during action, but also depth image with 320×240 pixels of each frame in videos are recorded. To avoid data redundancy, images were resized before performing calculations. As shown in Supplementary Figure 26a, the depth image (320×240 pixels) of each

设置了格式: 字体: 非倾斜

设置了格式: 字体: 非倾斜

设置了格式: 字体: Times New Roman, 三号

设置了格式: 字体: Times New Roman, 三号, 非倾斜

设置了格式: 字体: Times New Roman, 三号, 非倾斜

设置了格式: 字体: Times New Roman, 三号

设置了格式: 字体: Times New Roman, 三号, 非倾斜

设置了格式: 字体: Times New Roman, 三号

设置了格式: 字体: Times New Roman, 三号, 非倾斜

设置了格式: 字体: Times New Roman, 三号

设置了格式: 字体: Times New Roman, 三号

设置了格式: 字体: Times New Roman, 三号, 非倾斜

设置了格式: 字体: Times New Roman, 三号, 非倾斜

设置了格式: 字体: Times New Roman, 三号

设置了格式: 字体: Times New Roman, 三号

设置了格式: 字体: Times New Roman, 三号, 非倾斜

设置了格式: 字体: Times New Roman, 三号, 非倾斜

设置了格式: 字体: Times New Roman, 三号

设置了格式: 字体: Times New Roman, 三号, 非倾斜

设置了格式: 字体: Times New Roman, 三号

设置了格式: 字体: Times New Roman, 三号, 非倾斜

设置了格式: 字体: Times New Roman, 三号, 非倾斜

设置了格式: 字体: Times New Roman, 三号, 非倾斜

设置了格式: 字体: Times New Roman, 三号

设置了格式: 字体: Times New Roman, 三号

设置了格式: 字体: Times New Roman, 三号, 非倾斜

设置了格式: 字体: Times New Roman, 三号

设置了格式: 字体: Times New Roman, 三号

设置了格式: 字体: Times New Roman, 三号, 非倾斜

设置了格式: 字体: Times New Roman, 三号, 非倾斜

设置了格式: 字体: Times New Roman, 三号, 非倾斜

设置了格式: 字体: Times New Roman, 三号

设置了格式: 字体: Times New Roman, 三号

设置了格式: 字体: Times New Roman, 三号, 非倾斜

设置了格式: 字体: Times New Roman, 三号, 非倾斜

设置了格式: 字体: Times New Roman, 三号

设置了格式: 字体: Times New Roman, 三号

设置了格式: 字体: Times New Roman, 三号, 非倾斜

frame in videos was resized into image with 32×24 pixels, and then reshaped into a pixel sequence (size: 1×768). The pixel sequence (size: 1×768) of n th frame of the action video was multiplied by the mask matrix (size: 768× M), generating virtual nodes ($V_n=[\mathbf{V}_{n1} \ \mathbf{V}_{n2} \ \dots \ \mathbf{V}_{nM}]$) with a size of 1× M . In this case, the pixel sequence is mapped to a higher dimensional matrix noted as PreIn matrix. The subsequent calculation steps of GRF encoding and obtaining reservoir states for training and testing were consistent with the method for skeleton frames as mentioned in the manuscript. Supplementary Figure 26b shows partial example of obtained reservoir states. A high recognition accuracy of 92.35% on 27 action types can be achieved based on our bioinspired in-materia reservoir computing ($M=5$ and $L=100$), as shown in Supplementary Figure 26c, which has been verified by 5-time random subsampling validation method.

Supplementary Note 5. Noise-aware linear regression training method in Alpho-RC system

While implementing the weight mapping process with 1T1R array, noise interference is inevitable. In order to reduce the impact of noise on the recognition results, we implemented noise-aware linear regression training method. During training process, output weights are calculated by:

$$W_{\text{out}} = Y_{\text{target}}(X + N_{\text{tr}})^T ((X + N_{\text{tr}})(X + N_{\text{tr}})^T)^{\dagger} \quad (\text{S9})$$

where N_{tr} and X represent the applied noise and obtained reservoir states during training, respectively. During testing process combined with 1T1R array, the offline-trained weights are programmed into the memristor cells in the 1T1R array and output currents are obtained. During testing process in software simulations, the output is calculated by:

$$Y = (W_{\text{out}} + \max(|W_{\text{out}}|)N_{\text{te}})X \quad (\text{S10})$$

where N_{te} represents the noise level during weight mapping process with 1T1R array, which is estimated by:

$$N_{\text{te}} = \max(\frac{W_{\text{real}} - W_{\text{target}}}{W_{\text{target}}}) / \max(\frac{W_{\text{real}}}{W_{\text{target}}}) \quad (\text{S11})$$

where W_{real} and W_{target} represent the real weights and target weights while performing weight mapping.

In our experiment, noise level N_{te} is estimated of 0.0125 during weight mapping process with 1T1R array. Hence, N_{te} is a random matrix uniformly distributed between -0.0125 and 0.0125.

设置了格式: 字体: 非倾斜

N_{tr} is selected as Gaussian ~~white~~ noise with a mean value of 0 and a standard deviation value of 0.3.